Alireza Saeedmanesh

Department of Mechanical and Aerospace Engineering, University of California, Irvine, Irvine, CA 92697-3975 e-mail: asaeedma@uci.edu

Paolo Colombo

Department of Energy,
Politecnico di Torino,
Torino 10129, Italy
e-mail: paolo.colombo@studenti.polito.it

Dustin McLarty

School of Mechanical and Materials Engineering, Washington State University, Pullman, WA 99164-2920 e-mail: dustin.mclarty@wsu.edu

Jack Brouwer

Department of Mechanical and Aerospace Engineering, University of California, Irvine, Irvine, CA 92697-3975 e-mail: jbrouwer@uci.edu

Dynamic Behavior of a Solid Oxide Steam Electrolyzer System Using Transient Photovoltaic Generated Power for Renewable Hydrogen Production

This study investigates the dynamic behavior of a solid oxide steam electrolyzer (SOSE) system without an external heat source that uses transient photovoltaic (PV) generated power as an input to produce compressed (to 3 MPa) renewable hydrogen to be injected directly into the natural gas network. A cathode-supported crossflow planar solid oxide electrolysis (SOE) cell is modeled in a quasi-three-dimensional thermo-electrochemical model that spatially and temporally simulates the performance of a unit cell operating dynamically. The stack is composed of 2500 unit cells that are assumed to be assembled into identically operating stacks, creating a 300 kW electrolyzer stack module. For the designed 300 kW SOSE stack (thermoneutral voltage achieved at design steady-state conditions), powered by the dynamic 0-450 kW output of PV systems, thermal management and balancing of all heat supply and cooling demands is required based upon the operating voltage to enable efficient operation and prevent degradation of the SOSE stacks. Dynamic system simulation results show that the SOSE system is capable of following the dynamic PV generated power for a sunny day (maximum PV generated power) and a cloudy day (highly dynamic PV generated power) while the SOSE stack temperature gradient is always maintained below a maximum set point along the stack for both days. The system efficiency based upon lower heating value of the generated hydrogen is between 0-75% and 0-78% with daily hydrogen production of 94 kg and 55 kg for sunny and cloudy days, respectively. [DOI: 10.1115/1.4043340]

1 Introduction

California, with its abundant natural resources, is the leading state in terms of clean power in the entire United States, focusing upon developing renewable power generation systems, e.g., solar power generation to reduce emissions and improve air quality. In California, energy and environmental policies are strong, e.g., 33% and 50% of retail electricity sales by both retail sellers and publicly owned electric utilities must be met with renewable energy by 2020 and 2030, respectively. Also, the state's greenhouse gas emissions are required by law to be reduced to 40% below 1990 levels by 2030. These policies are the main driving forces for integrating renewable electricity generation technologies into the utility grid network and economy. In each of the last 3 years, about 2000 MW of solar capacity has been added and integrated into the California power grid, indicating great strides toward the reduction of carbon footprint in electricity generation. According to a California Energy Commission tracking progress report [1], at the end of 2017, 30% of 2017 retail electricity sales was generated with renewable resources in which solar and wind contributed together more than 60%. This illustrates that California is ahead of schedule regarding integrating renewable energies into the power grid. However, rapid penetration of inherently intermittent and sometimes unpredictable solar and wind resources leads to challenges for the grid regarding the dynamics of too much intermittent renewable electricity. One challenge occurs when insufficient immediate demand, controllable demand, or electricity storage is not available, which leads to renewable "over-generation."

Currently, in California, the most cost-effective and applicable solution for handling the large-scale over-generated electricity is to curtail over-generation, which can be concerning from a policy perspective. Curtailment happens when renewable electricity generation exceeds society's immediate needs and the grid operator does not allow that electricity onto the grid. Figure 1 displays the amount of renewable energy curtailment in California in recent years.² Gigawatt hours of curtailment in recent years encourage industrial and academic professionals to find efficient ways to store over-generated electricity. Electrolysis is a promising technology that converts electricity to hydrogen by splitting water into hydrogen and oxygen. As the magnitude of curtailment increases, and especially as the need for shifting renewable energy from season-toseason is required, hydrogen produced from huge amounts of excess electricity via electrolysis (power-to-gas (P2G)) can be utilized for energy storage purposes. P2G could be valuable to dynamically use renewably generated electricity to prevent wasting of so much renewable electricity and also for dynamic grid load-balancing purposes.

High-temperature electrolysis of steam via an solid oxide steam electrolyzer (SOSE) system is promising because of its potential higher efficiency compared with current electrolysis technologies. Much research has been carried out focusing upon the steady-state operation of solid oxide electrolysis cell (SOEC). Li et al. [2] carried out tests to evaluate the co-electrolysis performance of SOEC at an operating temperature range of 550–750 °C. Stoots et al. [3] presented studies on the high-temperature electrolysis carried out at the Idaho National Laboratory aimed at investigating the performance of co-electrolysis in solid oxide stacks at various operating

¹Corresponding author.

Manuscript received October 5, 2018; final manuscript received March 18, 2019; published online April 12, 2019. Assoc. Editor: Soumik Banerjee.

²www.caiso.com/Documents/HistoricalCurtailment

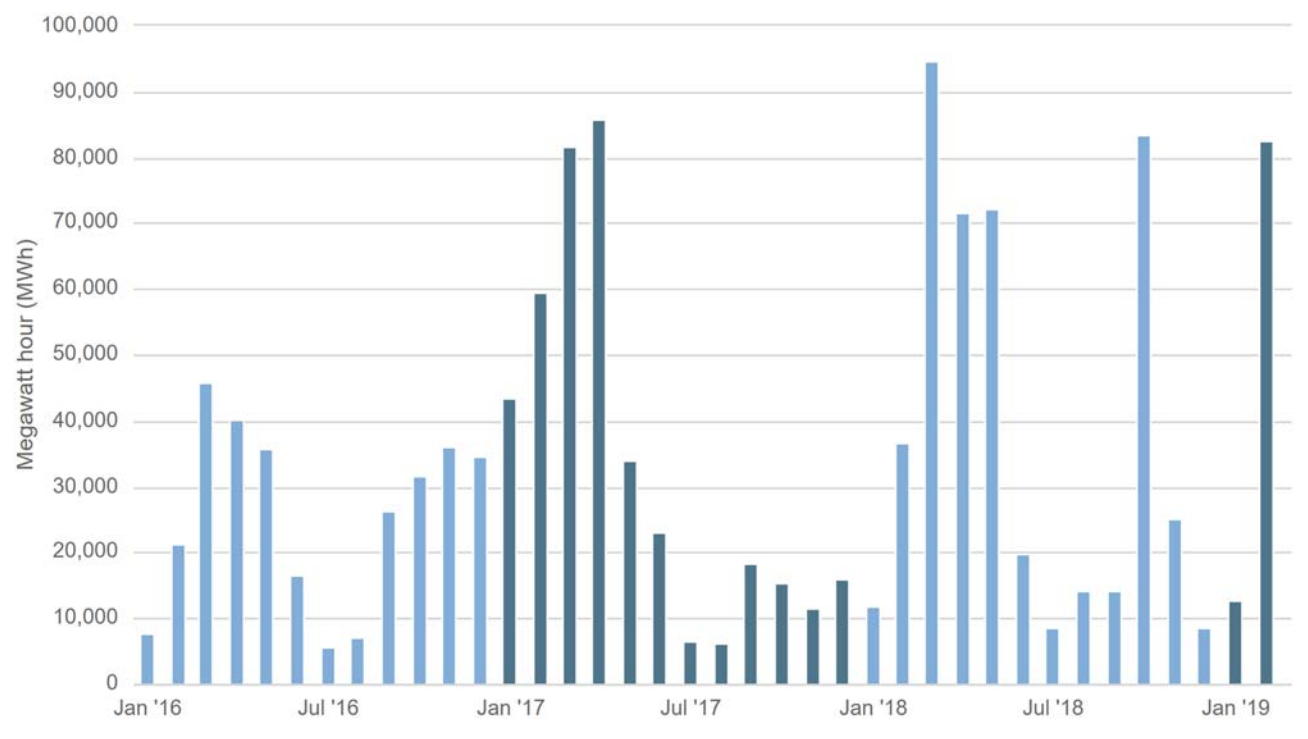


Fig. 1 California renewable curtailment³

conditions, e.g., temperature, gas mixture, and electrical settings. Graves et al. [4] focused on performance and durability analysis of co-electrolysis processes in solid oxide cells. Ni [5] developed two models to investigate the carbon dioxide electrolysis performance of SOEC at different levels. Ni [6] carried out another study regarding two-dimensional thermal modeling of a co-electrolysis process in an SOEC for syngas production. Ni et al. [7] conducted exergy and energy analysis to investigate thermodynamicelectrochemical behavior of an SOSE plant. Ni [8] developed a computational fluid dynamics model of an SOEC for hydrogen production. Grondin et al. [9] developed a multiphysics model aimed at investigating the performance and behavior of an SOEC. In another study from Grondin et al. [10], they developed a 3D simulation of an SOEC using an artificial neural network technique to simulate the cathodic process. Reytier et al. [11] carried out experiments on an SOEC at the stack level in both electrolysis and co-electrolysis modes. Penchini et al. [12] performed a theoretical study aimed at performance evaluation of a 200 W SOEC stack for hydrogen production. Stempien et al. [13] conducted an energy and exergy analysis of SOEC to evaluate the performance of the system and determine its optimal operating conditions.

In the literature, some studies have been carried out to evaluate the performance of SOE systems working at part load conditions. Sanz-Bermejo et al. [14] developed a complete model of an SOE system to evaluate and optimize the operation of the system at part load conditions operated under constant steam conversion or constant steam flow rate modes. Their results showed that the system has the capability to operate within the range of 10–100% power with 91–97% high heating value (HHV) efficiency, enabling the system to work with highly transient renewable energy sources. Also, they concluded that implementing constant steam conversion mode at low power loads and constant steam flow rate mode at high loads enabled broader operational power range with a flat performance curve. Sanz-Bermejo et al. [15] investigated the performance of an SOEC unit integrated with linear Fresnel reflector for grid management. They considered two different scenarios for their proposed system consisting of using SOEC system to produce hydrogen that

³See footnote 2.

was directly sold to a hydrogen refueling station, and storing the produced hydrogen from the SOEC, for later use in a solid oxide fuel cell (SOFC) for electricity generation. Petipas et al. [16] studied the steady-state behavior of an SOE system at different power loads considering no external heat source. They developed a zero-dimensional model composed of an SOE unit and balance of plant (BoP) to evaluate the performance of the system. They showed that when the system operated between 60% and 100% of design power, no temperature control is required, while for power below 60%, additional heating should be employed.

In the literature, some other studies were conducted to investigate the transient operation of SOEC. Petipas et al. [17] carried out tests on a single SOEC for both steady-state and transient conditions. They determined that the SOEC had the ability to operate under on-off conditions without any increase in degradation rate, which provides the ability of modular operation of SOEC with variable renewable power. Petipas et al. [18] developed a model which is composed of a zero-dimensional stack sub-model, BoP sub-model, and controller sub-model to investigate the behavior of an SOE system coupled with a solar farm. They showed that dynamic operation is technically feasible without implementing an external heat source. Their results revealed a production of 64.5 tons of compressed hydrogen using 2.76 GWh of the solar farm-generated electricity. Cai et al. [19] analyzed the dynamic response of an SOSE to transient inputs during renewable hydrogen production. A 1D dynamic model of an SOSE stack was developed to investigate the dynamic behavior of SOSE and to study the prospects for stack temperature control by variation of air flow rate. They impose step changes in current density, replicating a sudden change in electrical input energy or sudden switch off the SOSE stack. Another study from Cai et al. [20] proposed optimal control strategies for SOSE integrated with renewable energy. They considered different control strategies aimed at maximizing hydrogen production, while minimizing SOSE energy consumption or minimizing compressor energy consumption. Luo et al. [21] developed a 2D dynamic electrothermal model of steam and carbon dioxide co-electrolysis in a tubular SOEC. They studied the response of current, gas concentrations, temperature, and efficiency of the SOEC to electricity, gas flow, and temperature step inputs.

In this study, we develop a complete dynamic model to evaluate the dynamic behavior of a stand-alone SOSE system. The developed model consists of a quasi-3D model of the SOEC, which enables the investigation of the thermal gradients and thermal dynamics across the cell to evaluate the feasibility of operation under dynamic operating conditions. Furthermore, the entire SOSE system is modeled dynamically aiming at evaluating the behavior of all BoP components and taking into account all BoP power consumption to better figure out the performance of the proposed SOSE system. A control model is developed to control some operational parameters, e.g., operating temperature, the concentration of hydrogen at the cathode inlet stream to prevent oxidation of materials, and etc., by implementing some of the BoP components. Finally, the control strategies are evaluated by application of the SOSE system to measured solar photovoltaic (PV) power dynamics.

2 Physical Model Description

A SOSE system model has been developed in MATLAB software based upon a previously developed model in MATLAB/SIMULINK software at National Fuel Cell Research Center (NFCRC) [22,23]. The developed model is composed of a temporally and spatially resolved quasi-3D sub-model for an SOSE stack and BoP dynamic sub-models for different BoP components, such as heat exchangers, compressors, electric heaters, valves, and air blower.

2.1 SOSE Cell and Stack Model. The stack is composed of 2500 cathode-supported crossflow planar SOE unit cells that are assumed to be assembled into identically operating stacks, creating a 300-kW electrolyzer stack module. In the developed MATLAB model, a single repeating SOE unit cell is assumed to be representative of the behavior of all cells in each of the stacks. Therefore, the input and output flows and power are multiplied by the number of cells in the stack to obtain the stack values. The cell is modeled considering five different layers, i.e., steam side interconnects, steam flow channels, positive electrode-electrolyte-negative electrode (PEN), airflow channels, and air interconnect. In order to capture temporal and spatial behavior properties, various spatially distributed states are calculated at each time in time span using MATLAB ODE solver. In order to implement material and energy balances as well as polarization model, each layer is discretized into an 8×8 nodes and control volumes. In this study, the following assumptions are made on SOSE stack modeling:

- Electrochemical reactions occur instantaneously, due to fast kinetics of electrochemical reactions compared with thermal time scales.
- Electrical current only flows in one direction (from one electrode to the other along the PEN), due to the iso-potential electrode surfaces.
- Gases behave as an ideal gas, due to high operating temperature and atmospheric pressure operating conditions.
- Dynamic conservation equations apply to each gaseous nodal control volume. For each discretized gaseous nodal control volume, a continuously stirred tank reactor condition with the exit condition representing the condition throughout the control volume is assumed. These conditions include species concentration, temperature, and pressure.
- Both cathode and anode streams are in a laminar flow regime based upon the low Reynolds number in the flow channels, due to the low gas flow rate and the small cross-sectional area of the channels on both sides.
- Stack heat losses to the environment are neglected.

Figure 2 shows a schematic of a $10 \text{ cm} \times 10 \text{ cm}$ crossflow planar SOE unit cell.

2.1.1 Governing Equations. In this study, the governing equations can be expressed as shown in the following subsections.

2.1.1.1 Material conservation. The nodes related to cathode and anode flows present also species conservation balances needed to take into account the different species concentrations

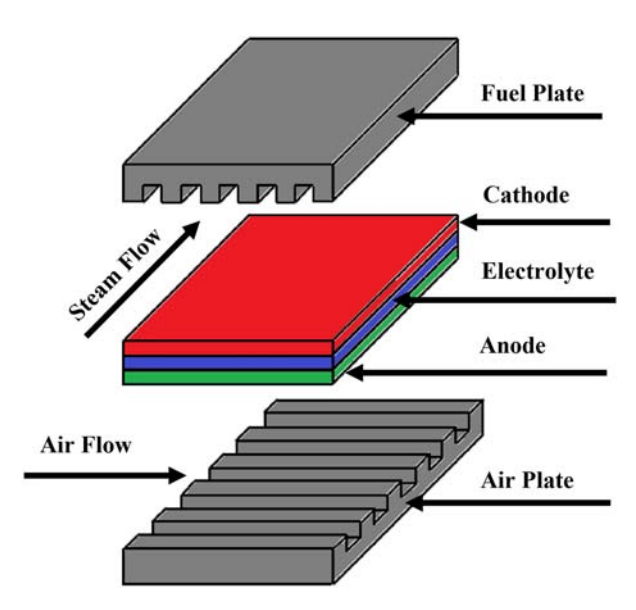


Fig. 2 Schematic of cross-flow SOE unit cell

along the flow channels. On the cathode side, the species are H_2 and H_2O , and species conservation is expressed in Eqs. (1) and (2), while on the anode side, the considered species are O_2 and O_2 , which are simulated by Eqs. (3) and (4) [22,23],

$$\frac{p_C \cdot V_C}{R \cdot T_C} \cdot \frac{d\chi_{H_2O}}{dt} = (\dot{n}_C \cdot \chi_{H_2O})_{In} - (\dot{n}_C \cdot \chi_{H_2O})_{Out} + \frac{I}{2F}$$
 (1)

$$\frac{p_C \cdot V_C}{R \cdot T_C} \cdot \frac{d\chi_{H_2}}{dt} = (\dot{n}_C \cdot \chi_{H_2})_{In} - (\dot{n}_C \cdot \chi_{H_2})_{Out} - \frac{I}{2F}$$
 (2)

$$\frac{p_A \cdot V_A}{R \cdot T_A} \cdot \frac{d\chi_{O_2}}{dt} = (\dot{n}_A \cdot \chi_{O_2})_{In} - (\dot{n}_A \cdot \chi_{O_2})_{Out} - \frac{I}{4F}$$
 (3)

$$\frac{p_A \cdot V_A}{R \cdot T_A} \cdot \frac{d\chi_{N_2}}{dt} = (\dot{n}_A \cdot \chi_{N_2})_{In} - (\dot{n}_A \cdot \chi_{N_2})_{Out} \tag{4}$$

where \dot{n} is the total molar flow rate in the anode or cathode channel node and χ is the species molar fraction, p, V, and T are the pressure, volume, and temperature of the respective channel node, and R is the gas constant. The current (I) is negative so that hydrogen and oxygen are yielded at the cathode and anode side, respectively, while steam is depleted at the cathode side.

2.1.1.2 Energy balance. Energy conservation equations for each control volume of the cathode channels, PEN layer, anode channels, and interconnect plates are presented in Eqs. (5)–(8) [22,23],

$$\rho_C \cdot c_{p_C} \cdot V_C \cdot \frac{dT_C}{dt} = \dot{Q}_T + \dot{H}_{In} - \dot{H}_{Out} + \dot{Q}_{Ion} - \dot{Q}_{React}$$
 (5)

$$\rho_{PEN} \cdot c_{PEN} \cdot V_{PEN} \cdot \frac{dT_{PEN}}{dt} = \dot{Q}_T + \dot{Q}_{GEN}$$
 (6)

$$\rho_A \cdot c_{p_A} \cdot V_A \cdot \frac{dT_A}{dt} = \dot{Q}_T + \dot{H}_{In} - \dot{H}_{Out} - \dot{Q}_{Ion} \tag{7}$$

$$\rho_{IC} \cdot c_{IC} \cdot V_{IC} \cdot \frac{dT_{IC}}{dt} = \dot{Q}_T \tag{8}$$

where \dot{H}_{ln} and \dot{H}_{Out} are the total enthalpy terms at the inlet and outlet condition of the gaseous nodes, respectively, ρ is the density, V is the volume, and c and c_p are the specific heat capacity.

 \dot{Q}_{lon} is the term related to the sensible enthalpy of the oxygen ions crossing the electrolyte from the cathode side to the anode side,

evaluated at PEN temperature according to Eq. (9).

$$\dot{Q}_{Ion} = \frac{I}{AF} \cdot h_{O_2} \tag{9}$$

 \dot{Q}_{GEN} is the term related to the heat generated or absorbed by the cell depending on the electrolysis thermodynamic behavior, evaluated according to Eq. (10).

$$\dot{Q}_{GEN} = \dot{Q}_{React} - V_{cell} \cdot I \tag{10}$$

 \dot{Q}_{React} is the heat of the reaction evaluated at PEN temperature with Eq. (11), V_{cell} is the cell operating voltage, and I is the current density of the node.

$$\dot{Q}_{React} = \frac{I}{2F} \cdot \left(h_{H_2} + \frac{1}{2} h_{O_2} - h_{H_2O} \right) \tag{11}$$

 \dot{Q}_T is the term related to convective and conductive heat transfer between solid–solid, solid–gaseous, and gaseous–gaseous interfaces.

$$\dot{Q}_T = \dot{Q}_{Cond} + \dot{Q}_{Conv} \tag{12}$$

The conductive heat transfer \dot{Q}_{Cond} is evaluated considering uniform surface temperature for both solid and gaseous nodes. The convective heat transfer \dot{Q}_{Conv} is calculated assuming laminar fully developed flow resulting in a constant Nusselt number.

2.1.1.3 Polarization model. The cell voltage is determined starting from the species concentrations in each node with the evaluation of the local Nernst potential according to Eqs. (13) and (14) [23],

$$V_{NERNST} = E_0 + \frac{R \cdot T_{PEN}}{2F} \cdot \ln \left(\sqrt{p_A} \cdot \frac{\chi_{H_2} \cdot \sqrt{\chi_{O_2}}}{\chi_{H_2O}} \right)$$
(13)

$$E_0 = \frac{-\Delta G_f}{2F} \tag{14}$$

where E_0 is the reversible voltage, ΔG_f is the molar change in Gibbs free energy of formation for water conversion to hydrogen and oxygen at the PEN nodal temperature T_{PEN} , and χ is the species molar fraction.

In this work, the cell polarization has been modeled to reproduce the behavior of recently developed high power density (HiPoD) solid oxide cells by Versa Power Systems (fuel cell energy). The materials used for these cells are conventional SOFC materials, with the cathode electrode made of nickel oxide and yttria-stabilized zirconia (YSZ), the electrolyte is YSZ, and the anode is all ceramic with no noble metals. The cells have a square geometry, and the flow channels of the metallic interconnect plates have a cross-flow arrangement [24,25]. The polarization curves have been acquired for three

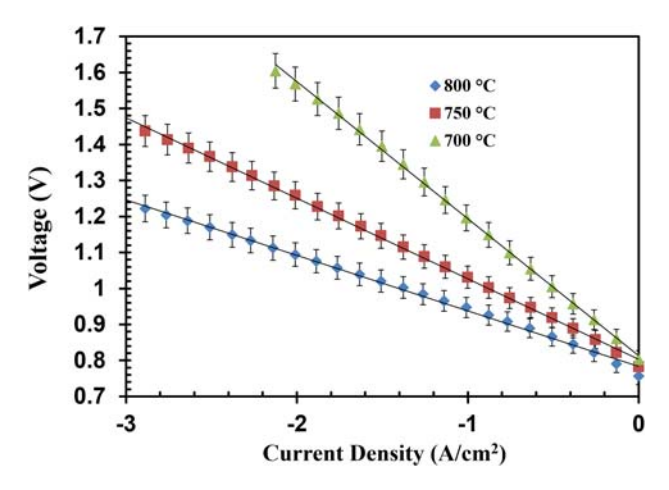


Fig. 3 Polarization curves of HiPoD cells [24]

Table 1 Polarization parameters

A	$4.64462 \times 10^{-5} \ \Omega \ \text{cm}^2$
В	$8.754 \times 10^{3} \text{ K}$ $0.1 \Omega \text{ cm}^{2}$
α	0.1 \$2 CIII

different operating temperatures of the cell. The curves can be well approximated by linear fit with an error lower than 4%, as shown in Fig. 3, allowing the determination of the area specific resistance (ASR) values at the three temperatures 700 °C, 750 °C, and 800 °C.

The equation for the overpotential of the cell has been derived with an exponential fitting of ASR values, expressed as Eq. (15). A similar approach can be found in many literature works [14,16,25].

$$ASR_{cell}(T_{PEN}) = A \times e^{B/T_{cell}}$$
 (15)

To take into account the increasing overpotential due to the interconnection of cells to form the stack, a constant value (α) has been added to the obtained equation for ASR [26].

$$ASR_{cell}(T_{PEN}) = A \cdot e^{B/T_{PEN}} + \alpha \tag{16}$$

The spatial overpotential and cell operating voltage are evaluated node-by-node with the following equations:

$$U = ASR_{cell}(T_{PEN}) \times j \tag{17}$$

$$V_{cell} = V_{NERNST} + U \tag{18}$$

where j is the current density of the node and V_{cell} is the cell operating voltage. Polarization model parameters are listed in Table 1.

2.2 Balance of Plant Components

2.2.1 Heat Exchanger. Heat exchangers are modeled as onedimensional counterflow plate heat exchangers composed of three layers, e.g., hot stream, metal separator plate, and cold stream in order to capture the thermal inertia of the heat exchangers. The developed dynamic model for a heat exchanger is spatially discretized into nodes and control volumes. In each node, material and energy balances are implemented using Eqs. (19) and (20),

$$\rho^{c,h} \cdot V^{c,h} \cdot c_p^{c,h} \cdot \frac{dT^{c,h}}{dt} = \dot{Q}_{conv} + \dot{H}_{In}^{c,h} - \dot{H}_{Out}^{c,h}$$
 (19)

$$\rho_{Plate} \cdot c_{Plate} \cdot V_{Plate} \cdot \frac{dT_{Plate}}{dt} = \dot{Q}_{conv}$$
 (20)

where \dot{Q}_{conv} is convective heat transfer between solid and gaseous nodes, ρ is the density, V is volume, and c_p and c are the specific heat capacity of gaseous and solid nodes.

2.2.2 Blower. A variable-speed blower model, enabling simulation of the inertia of the blower, is implemented in this study. The blower supplies sufficient pressure head and air flow rate not only for controlling the cell temperature but also for sweeping the produced oxygen at the anode side to prevent concentration losses. A minimum blower power of 0.5 kW is assumed in this study to always have air introduced toward the stack. The implemented dynamic model for the blower is shown in Eq. (21) [27],

$$J \cdot w \cdot \frac{dw}{dt} = P_B - P_{Imp} \tag{21}$$

where w is rotational speed, J is the moment inertia, P_B is the electric power supplied to the blower, and P_{Imp} is the impeller loss evaluated according to Eq. (22),

$$P_{Imp} = \frac{\dot{V}_{Air} \cdot \Delta P_{An}}{\eta_R} \tag{22}$$

Transactions of the ASME

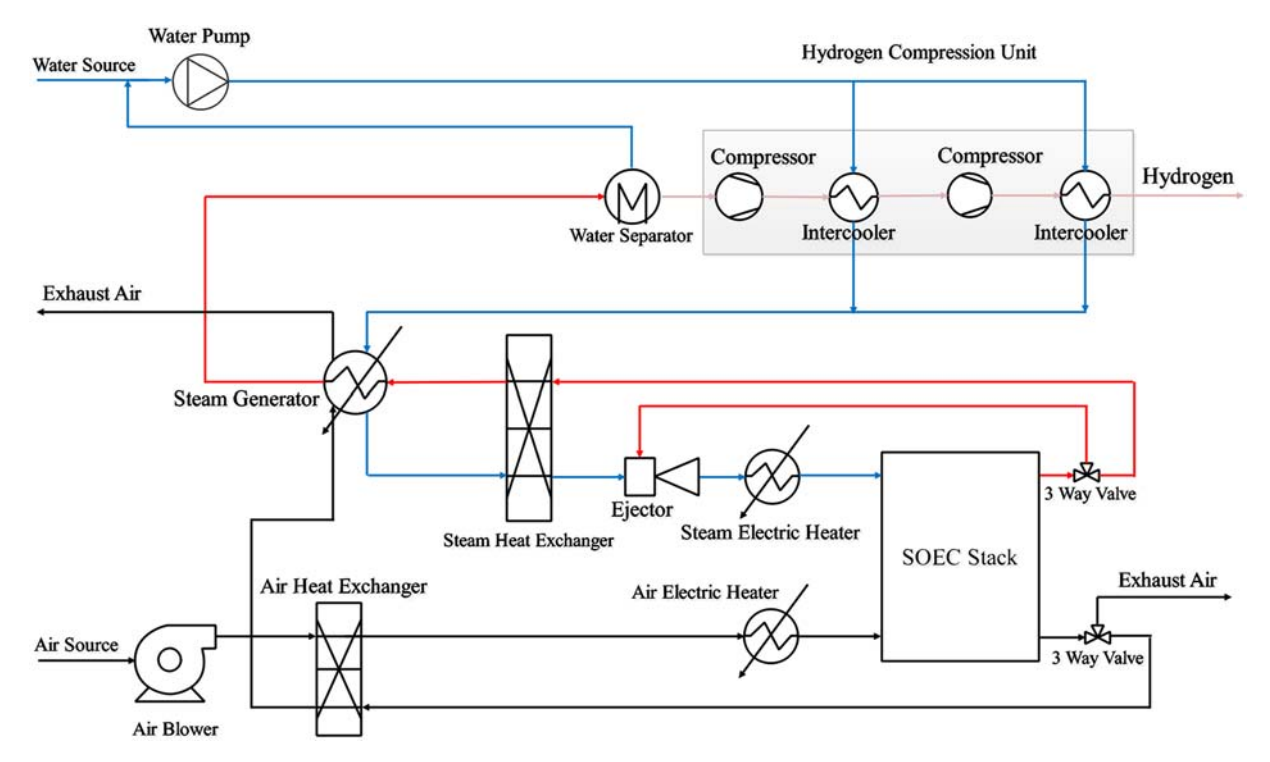


Fig. 4 SOSE system layout

where \dot{V}_{Air} is the air volumetric flow rate and ΔP_{An} is the pressure drop at the anode side and is the blower mechanical efficiency assumed 65% in this study.

2.3 System Layout. The system configuration has been developed to realize a stand-alone electrolysis system where the only energy input is electrical energy. Two inlet streams are present: the water stream and the ambient air stream. The system layout is presented in Fig. 4.

A pump feeds water at the required molar flow rate to the system by providing sufficient pressure head. Water is preheated in two-stage intercoolers of the hydrogen compressors. It then goes to the steam generator in which it evaporates using the recovered heats of stack cathode and anode outlet flows completed by the electric steam generator. The steam is additionally preheated using thermal energy from the hydrogen-rich stack outlet flow in a counter-flow plate heat exchanger. In the ejector, the steam flow is mixed with a partially recirculated cathode outlet flow to obtain 10% molar fraction of hydrogen at the cathode inlet to prevent oxidation of stack materials at high operating temperature. In order to bring the steam temperature to the desired stack inlet temperature, which is 1023 K in this study, an electric heater is implemented. The steam goes to the electrolyzer stack where the electrochemical reactions take place, resulting in a hydrogen-rich mixture at the stack outlet. A three-way valve is implemented, which is manipulated by a controller to recirculate a required portion of the outlet flow to have the desired hydrogen concentration at the cathode inlet. The hydrogen-rich stream heat is recovered in both heat exchanger and steam generator, then it is cooled further to below 60 °C to separate hydrogen from water in the water separator. The pure hydrogen is compressed in a two-stage compressor to reach 3 MPa to be injected directly into storage or natural gas pipelines. Air on the other side is introduced to the system by a variablespeed blower, which provides both the required mass flow rate and pressure head. It is preheated in a counter-flow plate heat exchanger and heated to the desired temperature by an electric heater to reach the desired temperature, which is 1023 K in this study. The anode outlet flow, which is enriched by the oxygen generated as a byproduct of the electrochemical reaction, passes through a heat exchanger and steam generator for heat recovery purposes.

2.4 System Performance. Once the system configuration was defined, the system performance can be evaluated considering system efficiency, stack efficiency, and voltage efficiency as defined in Eqs. (23)–(25), respectively,

$$\eta_{Sys} = \frac{\dot{n}_{H_2} \cdot LHV_{H_2}}{P_S + P_{EH,An} + P_{EH,Ca} + P_{SG} + P_P + P_B + P_{Comp}}$$
(23)

$$\eta_S = \frac{\dot{n}_{H_2} \cdot LHV_{H_2}}{P_S} \tag{24}$$

$$\eta_V = \frac{V_{Tn}}{V_{cell}} \tag{25}$$

where η is the efficiency, \dot{n}_{H_2} is the molar flow rate of produced hydrogen, LHV_{H_2} is the lower heating value of the hydrogen, P is the power consumption of different components, and V_{Tn} is the thermoneutral voltage at the stack operating temperature.

2.5 Control Strategy

Temperature Control. Cell temperature control is one of the key issues involved in the dynamic operation of hightemperature SOSE systems. In this study, the stack is thermally managed by manipulating one actuator, which controls the blower power. A variable speed blower enables control of blower dynamics that consider the inertia of the blower. Increasing the blower power ultimately increases the blower speed, which in turn increases the air flow rate introduced to the stack. The air flow rate has two functions in the proposed system, i.e., removing the oxygen produced as a byproduct of the electrochemical reactions and providing cooling or heating to the stack. The temperature control strategy consists of keeping the air inlet temperature and volumetric flow rate constant for a wide range of operating temperatures. In the developed control strategy, the cell average temperature is allowed to vary between maximum and minimum set-point values. When the difference between anode stream (air) outlet temperature and anode stream inlet temperature reaches one of the set-point constraints, the blower attempts to introduce more air in order to cool or heat the

NOVEMBER 2019, Vol. 16 / 041008-5

cell to keep the cell operating temperature difference inside the desired range. In this study, the controller set-point temperature difference constraint is 40 K. Also, the inlet temperature of both anode and cathode is controlled to the set point of 1023 K.

2.5.2 Power Control. The SOSE system is controlled by the electric power supplied to the stack. It is assumed that the power controller immediately adjusts the current for any change in stack input power as described by Eq. (26)

$$I = \frac{P_S}{V_{cell} \cdot N_{cell}} \tag{26}$$

where N_{cell} is the number of cells in SOSE stack.

2.5.3 Steam Flow Rate Control. The required feed water to the SOSE system is determined based upon Faraday's law of electrolysis and specified steam utilization as indicated below.

$$\dot{n}_{H_2O} = \frac{I}{2F} \cdot \frac{N_{Cell}}{SU} \tag{27}$$

where SU is the SOSE system steam utilization defined as the ratio between stoichiometric steam flow required for the electrochemical reactions at a given current and the actual inlet steam flow introduced to the system. A minimum steam flow of 2.7 g/s ensures that the steam entering the electrolyzer is of sufficient temperature. This constraint decreases the steam utilization at stack power outputs below 25 kW. A threshold of this nature is required for many high temperature electrolyzers, though the precise threshold will depend upon the specifics of the heat exchanger and hot box arrangement.

3 Problem Description

The University of California, Irvine (UCI) campus microgrid incorporates about 4 MW of solar PV. A 15-min resolution dataset for the operation of PV generation was obtained from a database that archives PV power dynamics of systems on the UCI campus. The dataset was scaled to a maximum of 450 kW of PV generation to consider the case where about 10% excess generated electricity is to be utilized by the SOSE system for renewable hydrogen production.

The PV generation dataset was analyzed to obtain a day in which the PV generated power has its highest dynamic behavior (a cloudy day) and another day in which the PV generated power is maximum (a sunny day). Figure 5 shows PV generated power for both the sunny day and the cloudy day.

The purpose of this study is to evaluate the capability of the SOSE system to effectively convert renewable electrical power into

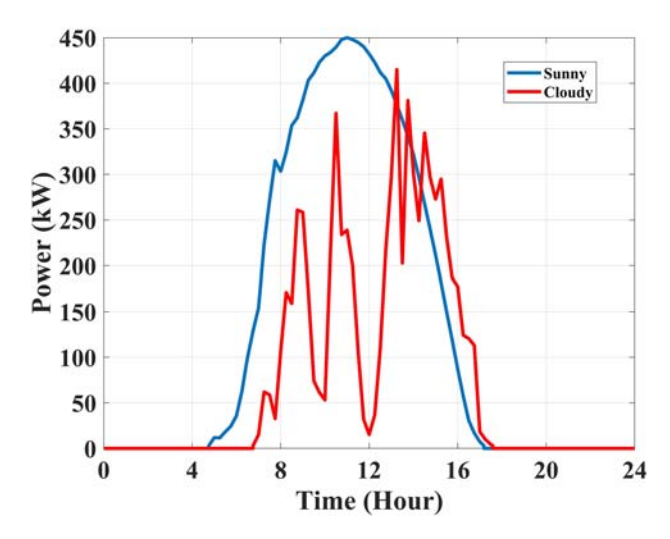


Fig. 5 PV generated power for a sunny and a cloudy day

hydrogen and to dynamically follow input power variations while maintaining all system variables within the acceptable limits. The obtained PV generated powers (Fig. 5) are given directly to the SOSE system to evaluate the performance of the SOSE system as it might be integrated with over-generated renewable PV power. The dynamic simulation of the SOSE system using measured dynamic power generation profiles for sunny and cloudy days as input to the system is exactly expected for a real-world application.

4 Results and Discussion

4.1 Steady-State Simulation. First, the developed SOSE system model is used to carry out a steady-state simulation on both stack level and system level to obtain not only the spatial distribution of different variables, e.g., Nernst voltage, overpotential, current density, and species concentration, but also the performance of the system at steady-state operating condition. The SOSE system is designed to operate at 1023 K temperature and thermoneutral voltage, which is 1.285 V at the design temperature. It should be noticed that the spatial distribution of both PEN operating temperature and operating voltage is obtained uniform with constant values 1023 K and 1.285 V, respectively.

Figure 6 shows the spatial distribution of Nernst voltage, overpotentials, and current density in a unit SOE cell. The Nernst voltages are among 0.89 V-1.03 V. The Nernst voltage has its highest amount at the corner close to the cathode and anode streams outlet and its lowest amount at the corner close to the cathode and anode streams inlet where both steam and air are fresh. The lowest amount of overpotentials is 0.26 V captured where the current density has its lowest absolute value (0.76 A/cm²) and the Nernst voltage has its highest value. On the other hand, the highest amount of overpotentials is 0.39 V, which corresponds to the highest absolute value of current density (1.15 A/cm²) and lowest Nernst voltage value.

Figure 7 shows the spatial distribution of different species' molar fractions. As shown, along the steam flow direction, the steam is consumed in the electrochemical reactions while the hydrogen is produced as a product of electrochemical reactions leading to lower steam and higher hydrogen molar fractions in the flow direction. The hydrogen concentration at the beginning of the cell is 10% which is imposed by a controller so that hydrogen present at the cathode inlet may prevent oxidation of stack materials at the high operating temperatures of an SOEC. At the cathode stream outlet, the hydrogen concentration is 80%, which results from the inlet composition and steam utilization to produce hydrogen. Along the anode stream flow direction, oxygen molar fraction increases due to oxygen production by the electrochemical reactions, also resulting in a decrease in nitrogen molar fraction. The oxygen concentration varies from 22% to 38%. This relatively high change in oxygen concentration along the anode flow direction is due to conditions of air flow rate that is at its minimum value associated with thermoneutral conditions. It should be noted that if the endothermicity or exothermicity of the electrochemical reactions is great enough, more air will be introduced to the SOEC stack (to cool or warm the stack) so that lower final oxygen concentrations will be achieved.

Table 2 presents the steady-state operating parameters of the developed SOSE system. Note that some electric heater power is required at this design condition due to the fact that some energy leaves the system with the produced hydrogen and oxygen/air streams.

4.2 Dynamic Simulation

4.2.1 Sunny Day. The PV generated power for a sunny day between 4:45 and 17:15 is directly given to the stack as an input power to capture the dynamic performance of the SOSE system.

Figure 8 shows both the PV generated power in the sunny day which is directly given to the stack and the SOE stack consumed power which is obtained by multiplying the operating voltage by the current and number of the cells. It shows that how closely the SOE system captures the transient behavior of the given power.

Transactions of the ASME

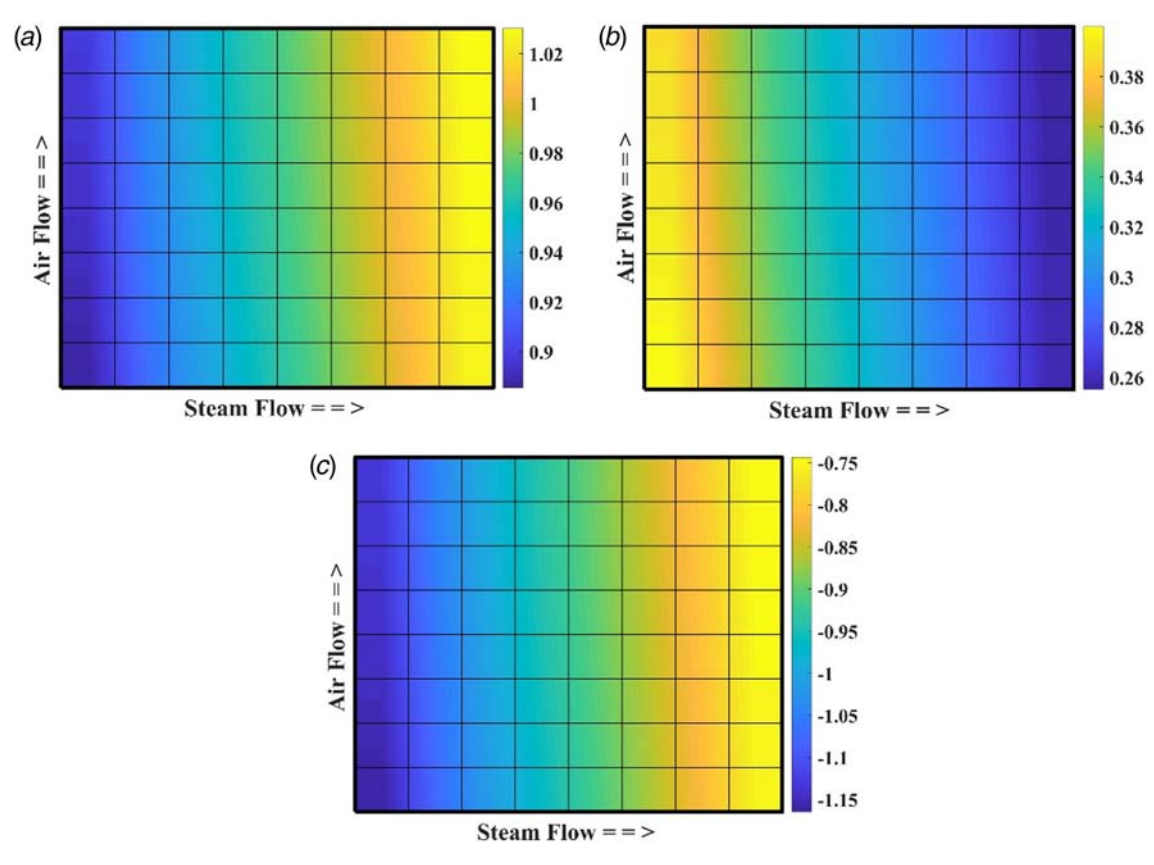


Fig. 6 Steady-state spatial distribution of (a) Nernst voltage (V), (b) overpotential loss (V), and (c) current density (A/cm²)

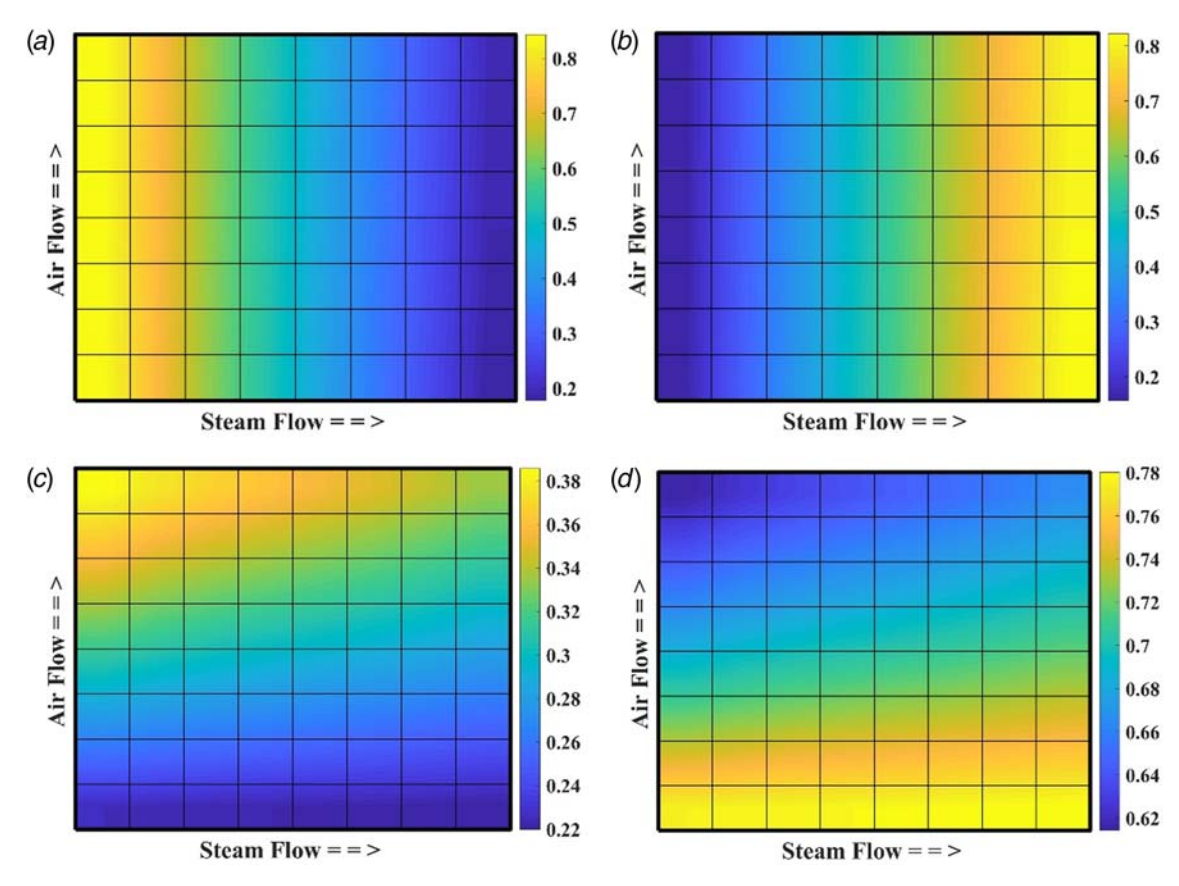


Fig. 7 Steady-state spatial distribution of the molar fraction of (a) steam, (b) hydrogen, (c) oxygen, and (d) nitrogen

Table 2 Steady-state operating parameters of SOSE system

Parameter	Value
Cell operating voltage (V)	1.285
Cell current density (A/cm ²)	0.93
Stack power (kW)	300
Steam utilization (–)	0.85
Steam electric heater power (kW)	10.5
Air electric heater power (kW)	7.1
Steam generator electric heater power (kW)	41.8
Blower power (kW)	0.5
Hydrogen compressor power (kW)	21.7
Pump power (kW)	2.1×10^{-4}
System efficiency (%) (based on LHV)	76.2
Hydrogen production (g/s)	2.4
Energy per kg H ₂ (kWh/kg H ₂)	43.8

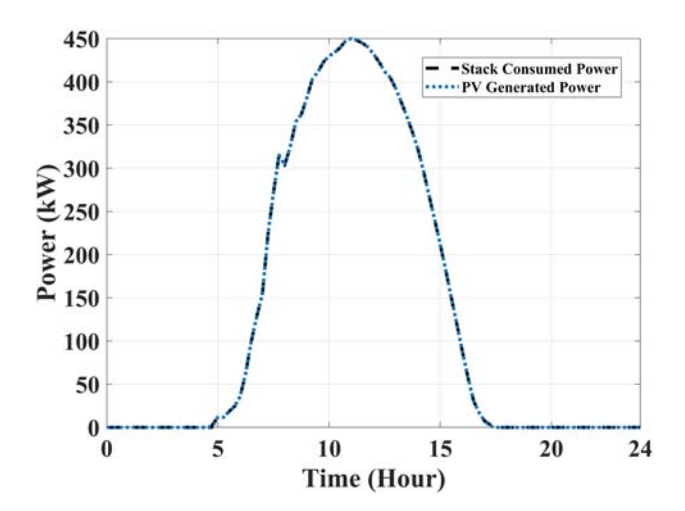


Fig. 8 PV generated power versus stack consumed power $(V_{Cell} \times I \times N_{Cell})$ for a sunny day

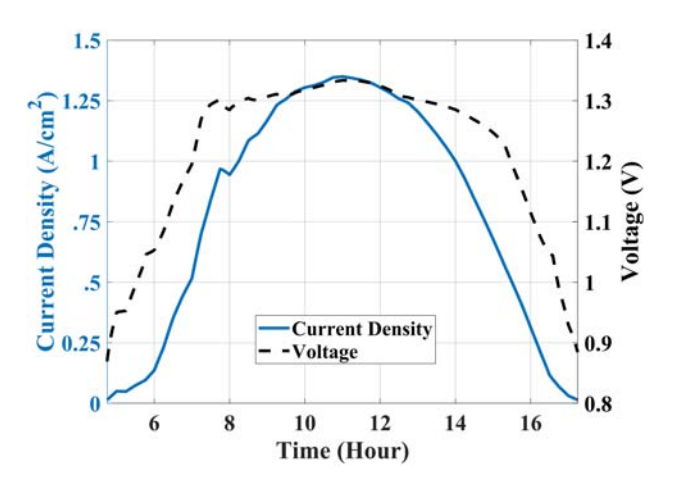


Fig. 9 Cell current density and voltage for a sunny day

Figure 9 shows that the cell current density varies in the range of 0–1.35 A/cm² and reaches its maximum value at about 11 exactly when the PV generated power has its maximum amount (Fig. 8). As displayed in Fig. 9, the cell operating voltage varies between 0.87 V and 1.33 V. The operating voltage begins in an endothermic region crossing the thermoneutral voltage at about 7:30 going to exothermal operating condition, and it goes back to endothermal operating condition at 14:30. These 7 h of operation include

conditions in which stack input power is higher than the nominal 300 kW stack power.

Figure 10 illustrates that the PEN average temperature varies between 985 K and 1062 K. It is assumed that at the beginning of system operation, the stack has a uniform temperature of 1023 K, which is the steady-state nominal operating condition at thermoneutral conditions so that the temperature difference along the PEN is zero. Early in the morning, during the startup, the PEN average temperature drops because of the endothermicity of the reactions below the thermoneutral point. At about 6:00, the PEN average temperature reaches its minimum level due to a period of operation in the high endothermicity region of the electrochemical reaction. Due to the large and continuous endothermicity at this time, the anode stream temperature difference reaches to 40 K (the controller set point). The thermal controller begins introducing more air flow to the SOE stack by manipulating the blower power. As a result, the cell average temperature is maintained between maximum and minimum set-point values (1023 K \pm 40 K). The minimum cell average temperature is 985 K which is about 40 K (controller set point) lower than the nominal operating temperature. However, increasing the air mass flow rate to maintain average cell temperature in the acceptable region causes a temperature gradient along the cell as shown in Fig. 10. The maximum temperature difference along the cell is 18 K, which is acceptable for SOEC dynamic operation in terms of resulting thermal stress. Figure 10 clearly shows how the temperature controller perfectly acts to maintain the cell average temperature between maximum and minimum set-point values (1023 K \pm 40 K) by manipulating the blower power. At about 7:30, when the operating voltage approaches the thermoneutral voltage, the PEN average temperature returns to 1023 K (the steady-state nominal operating temperature). Around 11:00, the SOEC is working in the highly exothermic operating condition, in which the temperature controller increases the blower power to maintain the temperature below 1062 K, which is about 40 K higher than the nominal operating point. At 11:00, the PEN average temperature and temperature difference along the PEN are close to their maximum value. As shown in Fig. 10, the thermal controller maintains the temperature in the range of ±40 K of the nominal operating temperature. The closer the voltage gets to the thermoneutral point, the more the PEN average temperature approaches the nominal operating point and the more uniform the temperature distribution becomes. Note also that the temperature difference along the PEN is zero when the stack is not operating and also whenever the cell operating voltage is close to the thermoneutral point. Note that both Figs. 9 and 10 provide evidence of the SOEC stack thermal inertia at around 7:30 when the cell operating voltage crosses the thermoneutral voltage. At this time, the stack average temperature is about

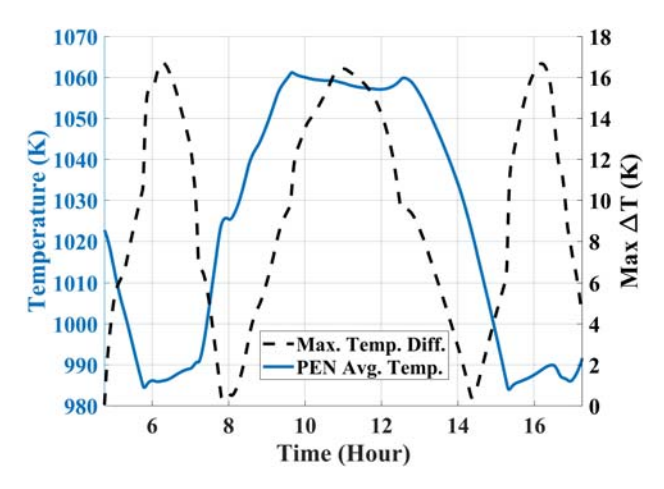


Fig. 10 PEN average temperature and maximum temperature difference along the PEN for a sunny day

997 K which is about 25 K lower than what is expected under thermoneutral operating conditions. Also, according to Fig. 10, there is a 6 K temperature difference along the stack at this moment (versus the uniform temperature that occurs under thermoneutral conditions at steady state). At around 7:45, the stack average temperature becomes 1023 K. It shows that although the operating voltage crosses thermoneutral voltage at 7:30, there is a 15-min delay for the stack, due to its thermal inertia, to reach 1023 K which is associated with the thermoneutral operating point.

Figure 11 shows the minimum, average, and maximum PEN temperature versus time. When the operating voltage is close to the thermoneutral point, all three temperatures are close to each other and equal to the nominal operating temperature. However, at highly endothermic and exothermic operating conditions, the deviation of minimum and maximum temperature from the average temperature increases which causes temperature gradient along the cell (as discussed regarding Fig. 10).

The good performance of the SOSE system is highlighted in Fig. 12, which indicates that the system efficiency throughout the majority of the operating time remains at values higher than 70% LHV. High efficiency is even achieved during the periods in which the current is high leading to high hydrogen production rate. The average efficiency of the SOSE system over the entire

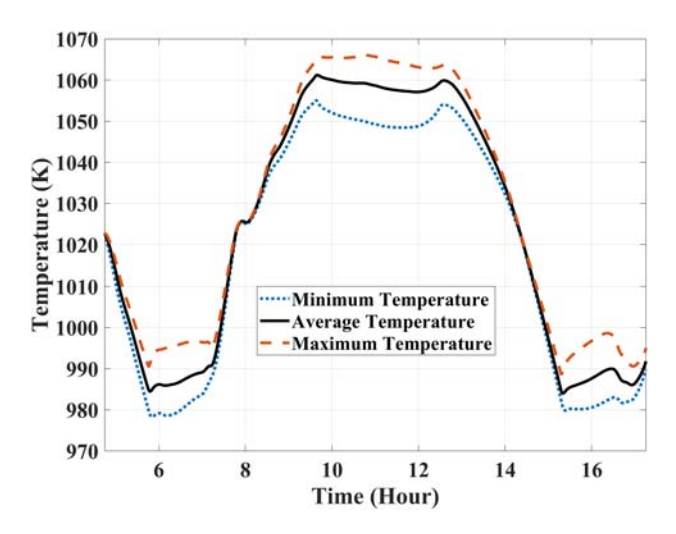


Fig. 11 PEN minimum, average, and maximum temperature for a sunny day

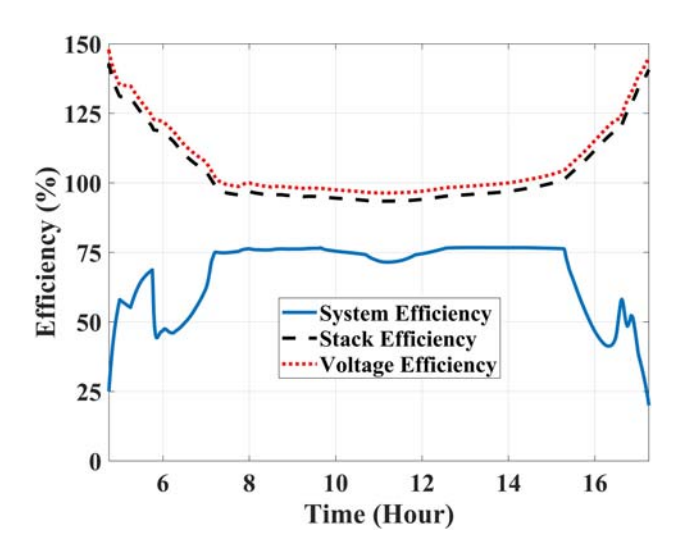


Fig. 12 Efficiencies for a sunny day

12.5 h of operation is 68%. It should be noted that between 7:30 and 15:30, the average system efficiency is 74%. According to Fig. 12, when the SOE system begins working, between 4:45 and 6:00, the system efficiency increases up to around 70%. Since the cell operating voltage is very low from 4:45 to 6:00, the endothermicity of the electrochemical reaction is very low, and as a result, the absolute change in both the average temperature of the cell and the anode stream temperature difference along the cell is less than 40 K (the controller set point). Hence, the system requires a minimum amount of air flow rate, and as a result, the blower power works at its minimum power. Also, low air flow rate needs low air electric heater power consumption. As a result, an increase in efficiency due to the increase in the amount of hydrogen produced can be observed. However, at around 6:00, the endothermicity of the cell causes an increase in anode stream temperature difference which is greater than the controller set point. So, the blower begins introducing more air into the system. This results in an increase in both the blower power consumption and air electric heater power consumption. Hence, a slight dip in the SOE system efficiency occurs at around 6:00. Between 7:00 and 10:00, the SOE system is working close to its thermoneutral voltage, and as a result, the endothermicity (for times the cell operating voltage is lower than the thermoneutral voltage) and exothermicity (for times the cell operating voltage is higher than the thermoneutral voltage) are not too much which causes the blower to be working around its minimum power setting and so minimal amounts of air are introduced to the anode side. Around 11:00, there is a slight drop in efficiency, which is due to the high operating voltage and high exothermicity operation of the cell. The high operating voltage pushes the controller to manipulate the blower power to increase the air flow rate to the anode side to maintain the anode stream temperature difference at the controller set point. After 15:00, when the PV generated power decreases, a drop in efficiency is obtained, which is due to the thermal controller function for highly endothermic conditions (similar to what happened at around 6:00). The controller pushes more air to the stack which increases both blower and air electric heater power consumption. The voltage and stack efficiencies have quite similar trends where the former varies between 96% and 148% while the latter varies between 93% and 142%. They are above 100% when the cell operating voltage is lower than the thermoneutral voltage and vice versa. It should be noticed that for the hours in which the stack efficiency is above 100% (the operating voltage is below the thermoneutral voltage (thermoneutral voltage is a voltage at which hydrogen and oxygen are produced with 100% thermal efficiency (i.e., no waste heat produced from the reaction))), the electric power given to the stack is lower than the energy of the produced hydrogen (based on LHV), since the electrolysis reaction is an endothermic reaction and the stack gets a portion of its required energy in a form of heat provided by electric heaters. Stack efficiency above 100% is significantly valuable in case of having available external heat sources that can be utilized to provide a portion of the required energy for an electrochemical reaction. This results in stack efficiency above 100% by utilizing the external heat source to produce hydrogen by consuming less electric energy. In a sunny day, during the 12.5 h of operation, the SOSE system consumes 4322 kWh and produces 94 kg of hydrogen.

Figure 13 shows the contribution of each SOSE component to the system power consumption. For the majority of the operating time, the stack power accounts for the highest consumed power. For 2.5 h at the beginning and at the end of the system operating time, the contribution of the air side electric heater increases not only due to the increased air flow rate for heating purposes but also due to the higher required temperature rise via air electric heater that results from lower heat recovered in the air side heat exchanger from lower temperature air leaving the stack. When the air electric heater consumed power increases, the steam generator power consumption decreases because of increased air heat recovery in the steam generator. In the middle of the day, when the stack is operating in the highly exothermic region, the air electric heater power

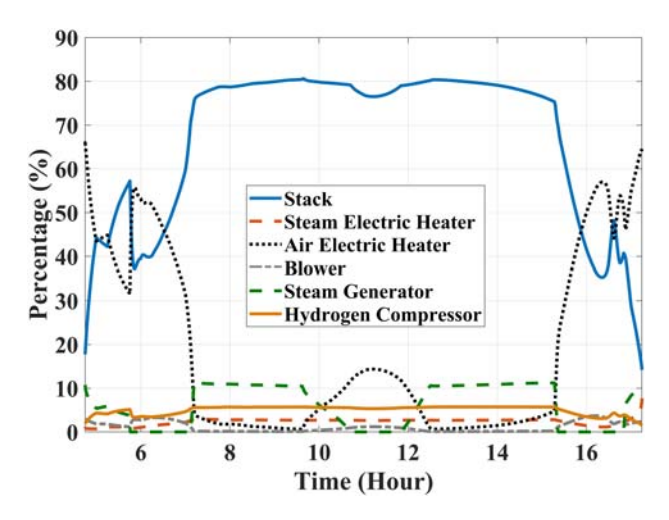


Fig. 13 Contribution of each component in power consumption for a sunny day

consumption increases (nonintuitively) to maintain air inlet temperature while increasing airflow to provide adequate cooling to the stack.

Figure 14 shows the spatial distribution of current density, overpotential voltage, temperature, and oxygen concentration at around 6:00, in which the SOEC exhibits its minimum average temperature and maximum temperature difference along the cell. This operating condition is the highly endothermic condition in which the operating voltage is between the open circuit voltage and the thermoneutral

voltage. The operating voltage at this most endothermic operating condition is 1.1 V. According to Fig. 14, the spatial overpotential loss varies from 0.06 V to 0.18 V which is lower than that of steady-state operating conditions (Fig. 6) and results from operating in this regime at lower current density. Moreover, the spatial temperature at this case varies from 979 K to 995 K while the highest and lowest spatial temperatures are located at the cell corners. As shown in Fig. 14, the oxygen concentration changes only slightly due to controller action to introduce large amounts of air to warm the cell. Since in this case, the endothermicity is high, the blower pushes more air to keep the anode stream temperature difference at the controller set point. As a result, the amount of oxygen produced in the electrochemical reaction is almost negligible compared with the amount of oxygen entering the anode.

Figure 15 shows the spatial distribution of operating parameters at around 11:00, in which the system is working at its maximum average temperature. This operating condition is the highly exothermic condition in which the operating voltage is greater than the thermoneutral voltage. The operating voltage at this endothermic operating condition is 1.33 V. According to Fig. 15, the spatial overpotential loss varies from 0.31 V to 0.45 V, which is higher than that of steady-state conditions (Fig. 6) resulting from high current density. Moreover, the spatial temperature at this case varies from 1050 K to 1066 K which is greater than nominal operating temperature conditions. As shown in Fig. 15, the oxygen concentration changes more compared with the endothermic condition shown in Fig. 14. This small change results from the controller that introduces more air to cool the stack because endothermicity is high. The small, but larger, change in oxygen concentration in the anode compartment compared with the endothermic condition is due to the higher current density and higher oxygen production

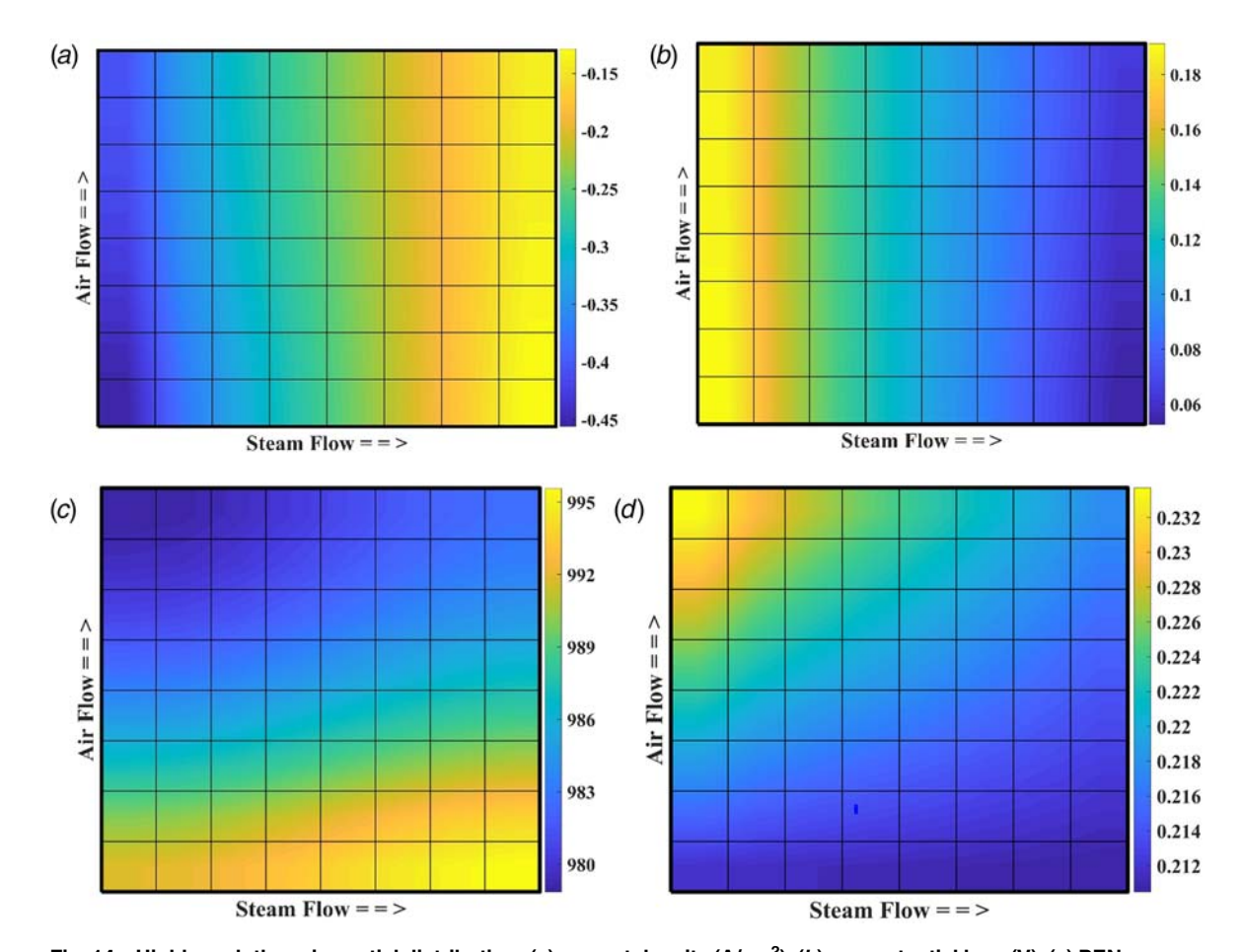


Fig. 14 Highly endothermic spatial distribution: (a) current density (A/cm²), (b) overpotential loss (V), (c) PEN average temperature (K), and (d) oxygen molar fraction

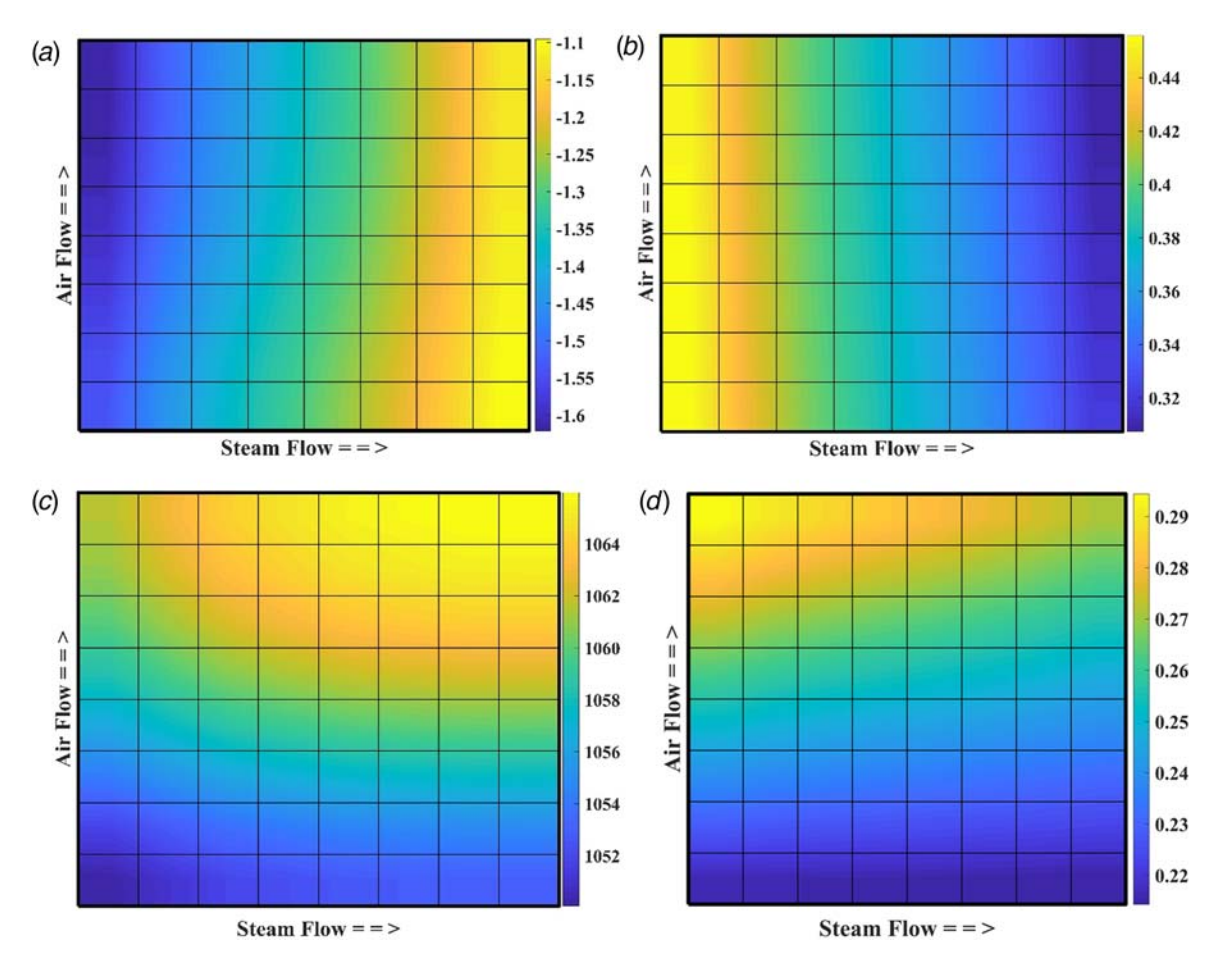


Fig. 15 Highly exothermic spatial distribution: (a) current density (A/cm²), (b) overpotential loss (V), (c) PEN average temperature (K), and (d) oxygen molar fraction

by the electrochemical reactions. However, the variation of oxygen concentration is lower compared with the steady-state operating condition (thermoneutral condition), since in the exothermic condition, the blower introduces more air to the anode to control the temperature of the stack.

4.2.2 Cloudy Day. The PV generated power for a cloudy day between 6:45 and 17:45 is directly given to the stack as an input power to capture the dynamic performance of the SOSE system. During the cloudy day, several strong dynamic conditions are present but nevertheless the system is able to modulate its operating condition following the highly dynamic renewable excess power. The transients related to the passing clouds cause multiple fluctuations of the cell operating voltage during the day rapidly switching between exothermic and endothermic modes of operation ten times.

Figure 16 shows both the PV generated power in the cloudy day which is directly given to the stack and the SOE stack consumed power which is obtained by multiplying the operating voltage by the current and number of the cells. It shows that how closely the SOE system captures the transient behavior of the given power.

As presented in Fig. 17, the cell operating voltage varies between 0.87 and 1.33 V, while the cell current density varies between 0 and 1.25 A/cm² and reaches its maximum value at about 13:25 exactly when the PV generated power has its maximum amount (Fig. 16). It should be noticed that due to the lower amount of PV generated power in this cloudy day scenario compared with the sunny day scenario, the SOEC is working mostly in endothermic and endothermal operating conditions.

Figure 18 shows multiple dynamic fluctuations in both PEN average temperature and maximum temperature difference along

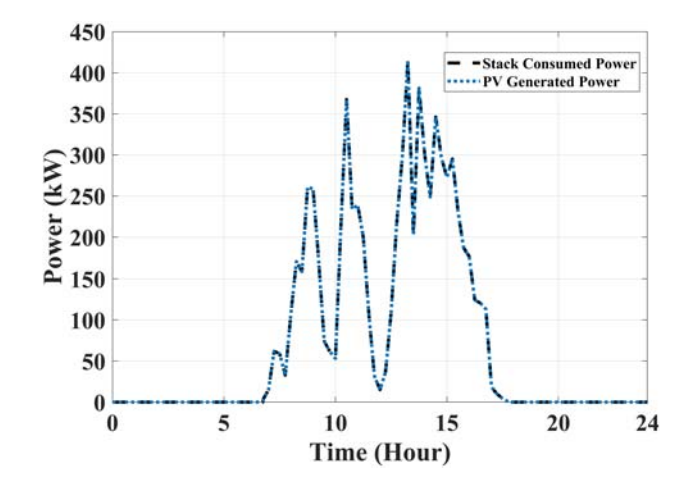


Fig. 16 PV generated power versus stack consumed power $(V_{Cell} \times I \times N_{Cell})$ for a cloudy day

the PEN. These variations are within safe operating limits, confirming the appropriate system configuration and appropriate applied temperature control strategy that is able to keep the stack operating temperature inside the 80 K safe range during realistic and highly dynamic operating conditions. The maximum temperature difference across the PEN is lower than 18 K. It is shown that the maximum PEN temperature difference increases when the PEN average temperature reaches its lower limit value. According to Fig. 18, for the cloudy day scenario, the PEN average temperature reaches its lower limit (40 K below 1023 K) during endothermic

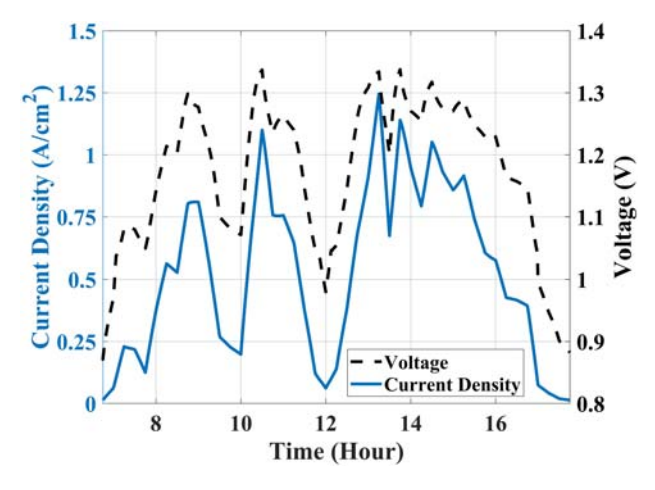


Fig. 17 Cell current density and voltage for a cloudy day

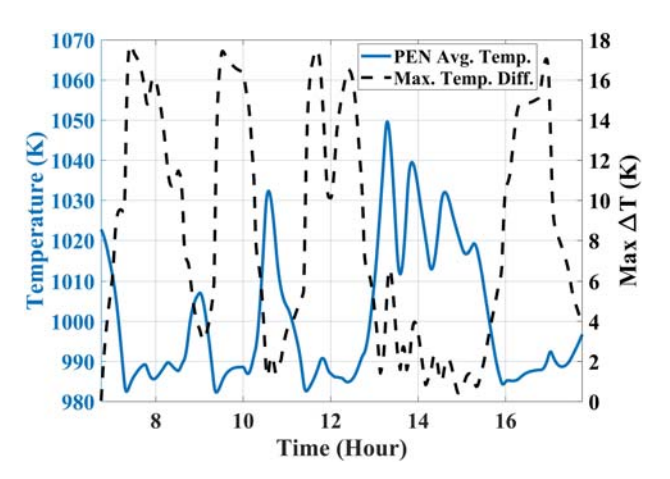


Fig. 18 PEN average temperature and maximum temperature difference along the PEN for a cloudy day

operating conditions since it stays in endothermic condition for a considerable time. However, it does not reach to its upper limit (40 K higher than 1023 K) because the SOE system does not stay in the exothermic operating condition for a very long time. Thus, the SOEC stack does not have enough time to heat up to the upper limit due to its thermal inertia. It should be noted that when the operating voltage is switched between endothermic and exothermic conditions, the SOEC stack takes time to experience dynamic changes in its temperature. In the cloudy day scenario, even though at several moments, the operating voltage crosses the thermoneutral condition toward exothermic conditions, the short duration of stay in exothermic mode does not allow the temperature of the stack to reach the upper safe limit. According to Fig. 19, the maximum and minimum temperatures of PEN have their highest deviation from the average temperature under highly endothermic operating conditions, while there is a small deviation obtained in moderate exothermic operating conditions.

The system efficiency for the cloudy day fluctuates a lot due to the fluctuations in stack input power (Fig. 20). The average efficiency of the SOSE system for the 11 h of operation is 63%. The voltage and stack efficiencies have quite similar trends where the former varies between 96% and 148% while the latter varies between 93% and 142%. Both of the stack and voltage efficiencies are above 100% for the majority of the time due to the operating voltage which is lower than the thermoneutral voltage most of the time. During the 11 h of operation, the SOSE system consumes 2663 kWh and produces 55 kg of hydrogen.

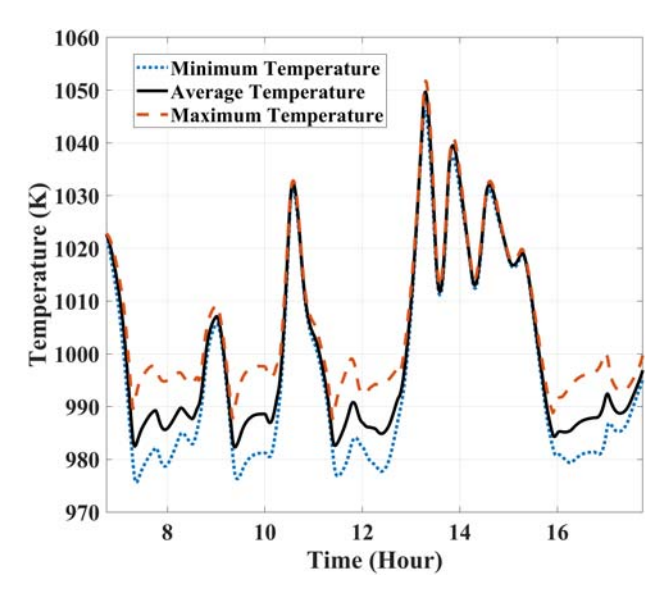


Fig. 19 PEN minimum, average, and maximum temperature for a cloudy day

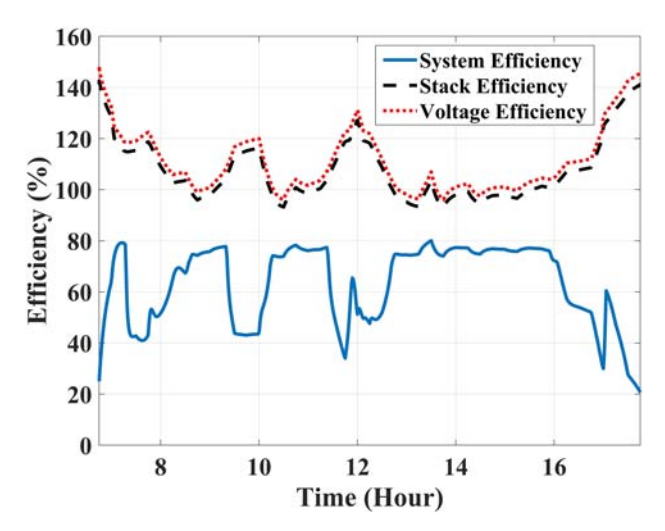


Fig. 20 Efficiencies for a cloudy day

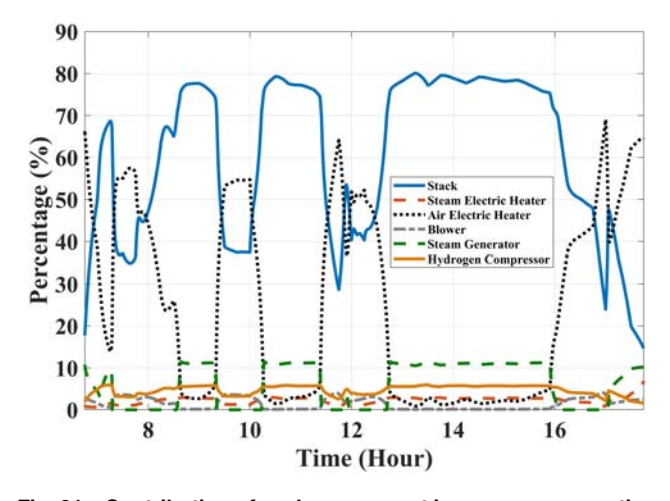


Fig. 21 Contribution of each component in power consumption for a cloudy day

041008-12 / Vol. 16, NOVEMBER 2019

Transactions of the ASME

Figure 21 shows the contribution of each SOSE component in the total system power consumption. As clearly shown in Fig. 21, the blower power and therefore the air electric heater power contributions increase four times throughout the day, corresponding to hours in which the cell operating temperature reaches its lower limit and the controller forces the blower to blow more air toward the SOSE stack to heat the stack. For most of the hours that correspond to the increased contribution of the air electric heater to overall power consumption, the contribution of the steam generator drops due to the higher air heat recovered in the steam generator. The highest stack power contribution happens between 13:00 and 15:00 where the PV generated power given to the stack has its maximum amount (Fig. 16), and the blower power is at its minimum power.

5 Summary and Conclusions

This study focused on evaluating the dynamic behavior of a SOSE system without an external heat source which uses transient PV generated power as an input to produce compressed (to 3 MPa) renewable hydrogen to be stored or injected directly into the natural gas network. The study developed an SOSE system design and control strategy and demonstrated that the proposed SOSE system is able to operate dynamically to directly convert solar power to hydrogen for both sunny and cloudy days. For the entire operating periods of both of these days, the stack temperature and temperature difference along the stack were maintained in a safe operating range. The 12.5 h operation of the SOSE system on a sunny day resulted in the production of 94 kg hydrogen by using an average of 46 kWh/kg of the produced hydrogen. The SOSE system operated 11 h on a cloudy day and produced 55 kg hydrogen at average system power consumption per kilogram of produced hydrogen of 48.4 kWh/kg. The temperature distribution and dynamics of temperature gradients (spatial and temporal) that our dynamic model has produced, as demonstrated in this paper, will have a significant impact on degradation and other performance characteristics. The impacts on degradation will be studied in future works.

Funding Data

 The authors acknowledge the National Science Foundation (NSF) under the Integrated Food Energy Water Systems (INFEWS) Program (Award No. 1639318) for partial support of this work.

Nomenclature

c = specific heat capacity (kJ/kg K)

h = specific enthalpy (kJ/kmol)

 $j = \text{current density } (A/\text{cm}^2)$

p = pressure (kPa)

t = time (s)

F = Faraday constant 96,485 (C/mol)

I = current (A)

P = electrical power (kW)

R = universal gas constant 8.314 (kJ/kmol K)

 $T = \text{temperature } (^{\circ}\text{C})$

U = overpotential(V)

 $V = \text{volume (m}^3)$

 $\dot{n} = \text{molar flow rate (mol/s)}$

 \dot{H} = total enthalpy of a stream (kW)

Q = heat flux (kW)

 \dot{V} = volume flow rate (m³/s)

 c_p = specific heat capacity at constant pressure (kJ/kg K)

 h_{conv} = convective heat transfer coefficient (W/m²)

 E_0 = cell reversible voltage (V)

 N_{cell} = number of cells in SOSE stack

 V_{cell} = cell operating voltage (V)

 V_{Nernst} = Nernst voltage (V)

ASR = area specific resistance (Ω cm²)

LHV = lower heating value (J/mol)

 ΔG = molar Gibbs free energy difference (kJ/mol)

 $\eta = \text{efficiency}(-)$

 $\rho = \text{density (kg/m}^3)$

 $\chi = \text{molar fraction } (-)$

Subscripts

A =anode stream

An =anode side

B = blower

C = cathode stream

Ca = cathode side

Comp = compressor

Cond = conduction

Conv = convection

EH = electric heater

IC = interconnector *Imp* = impeller

In = inlet

Ion = oxygen ions

Out = outlet

P = pump

PEN = positive electrode-electrolyte-negative electrode

React = reaction

S = stack

SG = steam generator

SU = steam utilization

Sys = SOSE system

T = total

Tn = thermoneutral

V = voltage

Superscripts

C = cold stream

H = hot stream

References

- California Energy Commission, 2017, California Energy Commission Tracking progress, renewable energy Overview.
- [2] Li, W., Wang, H., Shi, Y., and Cai, N., 2013, "Performance and Methane Production Characteristics of H₂O-CO₂ Co-Electrolysis in Solid Oxide Electrolysis Cells," Int. J. Hydrogen Energy. 38(25), pp. 11104–11109.
- Electrolysis Cells," Int. J. Hydrogen Energy, 38(25), pp. 11104–11109.
 [3] Stoots, C., O'Brien, J., and Hartvigsen, J., 2009, "Results of Recent High Temperature Co-Electrolysis Studies at the Idaho National Laboratory," Int. J. Hydrogen Energy, 34(9), pp. 4208–4215.
- [4] Graves, C., Ebbesen, S. D., and Mogensen, M., 2011, "Co-Electrolysis of CO₂ and H₂O in Solid Oxide Cells: Performance and Durability," Solid State Ionics, 192(1), pp. 398–403.
- [5] Ni, M., 2010, "Modeling of a Solid Oxide Electrolysis Cell for Carbon Dioxide Electrolysis," Chem. Eng. J., 164(1), pp. 246–254.
- [6] Ni, M., 2012, "2D Thermal Modeling of a Solid Oxide Electrolyzer Cell (SOEC) for Syngas Production by H₂O/CO₂ Co-Electrolysis," Int. J. Hydrogen Energy, 37(8), pp. 6389–6399.
- [7] Ni, M., Leung, M. K., and Leung, D. Y., 2007, "Energy and Exergy Analysis of Hydrogen Production by Solid Oxide Steam Electrolyzer Plant," Int. J. Hydrogen Energy, 32(18), pp. 4648–4660.
- [8] Ni, M., 2009, "Computational Fluid Dynamics Modeling of a Solid Oxide Electrolyzer Cell for Hydrogen Production," Int. J. Hydrogen Energy, 34(18), pp. 7795–7806.
- [9] Grondin, D., Deseure, J., Brisse, A., Zahid, M., and Ozil, P., 2008, "Multiphysics Modeling and Simulation of a Solid Oxide Electrolysis Cell," Proceedings of the COMSOL Conference, Hannover, Germany, Nov. 4–6.
- [10] Grondin, D., Deseure, J., Ozil, P., Chabriat, J.-P., Grondin-Perez, B., and Brisse, A., 2013, "Solid Oxide Electrolysis Cell 3D Simulation Using Artificial Neural Network for Cathodic Process Description," Chem. Eng. Res. Des., 91(1), pp. 134–140.
- [11] Reytier, M., Di Iorio, S., Chatroux, A., Petitjean, M., Cren, J., De Saint Jean, M., Aicart, J., and Mougin, J., 2015, "Stack Performances in High Temperature Steam Electrolysis and Co-Electrolysis," Int. J. Hydrogen Energy, 40(35), pp. 11370– 11377
- [12] Penchini, D., Cinti, G., Discepoli, G., and Desideri, U., 2014, "Theoretical Study and Performance Evaluation of Hydrogen Production by 200 W Solid Oxide Electrolyzer Stack," Int. J. Hydrogen Energy, 39(17), pp. 9457–9466.

NOVEMBER 2019, Vol. 16 / 041008-13

- [13] Stempien, J. P., Ding, O. L., Sun, Q., and Chan, S. H., 2012, "Energy and Exergy Analysis of Solid Oxide Electrolyser Cell (SOEC) Working as a CO₂ Mitigation Device," Int. J. Hydrogen Energy, 37(19), pp. 14518–14527.
- [14] Sanz-Bermejo, J., Muñoz-Antón, J., Gonzalez-Aguilar, J., and Romero, M., 2015, "Part Load Operation of a Solid Oxide Electrolysis System for Integration With Renewable Energy Sources," Int. J. Hydrogen Energy, 40(26), pp. 8291–8303.
- [15] Sanz-Bermejo, J., Gallardo-Natividad, V., González-Aguilar, J., and Romero, M., 2014, "Coupling of a Solid-Oxide Cell Unit and a Linear Fresnel Reflector Field for Grid Management," Energy Procedia, 57, pp. 706–715.
 [16] Petipas, F., Brisse, A., and Bouallou, C., 2013, "Model-Based Behaviour of a
- [16] Petipas, F., Brisse, A., and Bouallou, C., 2013, "Model-Based Behaviour of a High Temperature Electrolyser System Operated at Various Loads," J. Power Sources, 239, pp. 584–595.
- [17] Petipas, F., Fu, Q., Brisse, A., and Bouallou, C., 2013, "Transient Operation of a Solid Oxide Electrolysis Cell," Int. J. Hydrogen Energy, 38(7), pp. 2957–2964.
 [18] Petipas, F., Brisse, A., and Bouallou, C., 2015, "Modelled Behavior of a High
- [18] Petipas, F., Brisse, A., and Bouallou, C., 2015, "Modelled Behavior of a High Temperature Electrolyser System Coupled With a Solar Farm," Chem. Eng. Trans., 45, pp. 1015–1020.
- [19] Cai, Q., Brandon, N. P., and Adjiman, C. S., 2010, "Modelling the Dynamic Response of a Solid Oxide Steam Electrolyser to Transient Inputs During Renewable Hydrogen Production," Front. Energy Power Eng. China, 4(2), pp. 211–222.
- [20] Cai, Q., Adjiman, C. S., and Brandon, N. P., 2014, "Optimal Control Strategies for Hydrogen Production When Coupling Solid Oxide Electrolysers With Intermittent Renewable Energies," J. Power Sources, 268, pp. 212–224.

- [21] Luo, Y., Shi, Y., Li, W., and Cai, N., 2015, "Dynamic Electro-Thermal Modeling of Co-Electrolysis of Steam and Carbon Dioxide in a Tubular Solid Oxide Electrolysis Cell," Energy, 89, pp. 637–647.
- [22] McLarty, D., Brouwer, J., and Samuelsen, S., 2013, "A Spatially Resolved Physical Model for Transient System Analysis of High Temperature Fuel Cells," Int. J. Hydrogen Energy, 38(19), pp. 7935–7946.
- [23] McLarty, D., Samuelsen, S., and Brouwer, J., 2010, "Novel Dynamic Quasi-3-Dimensional High Temperature Fuel Cell Model with Internal Manifolding," Proceedings of the ASME Fuel Cell Science, Engineering and Technology, Brooklyn, New York, June 14–16, American Society of Mechanical Engineers.
- [24] Wood, A., He, H., Joia, T., Krivy, M., and Steedman, D., 2016, "Communication—Electrolysis at High Efficiency With Remarkable Hydrogen Production Rates," J. Electrochem. Soc., 163(5), pp. F327–F329.
- [25] Giglio, E., Lanzini, A., Santarelli, M., and Leone, P., 2015, "Synthetic Natural Gas Via Integrated High-Temperature Electrolysis and Methanation: Part I— Energy Performance," J. Energy Storage, 1, pp. 22–37.
- [26] Ferrero, D., Lanzini, A., Santarelli, M., and Leone, P., 2013, "A Comparative Assessment on Hydrogen Production From Low-and High-Temperature Electrolysis," Int. J. Hydrogen Energy, 38(9), pp. 3523–3536.
- [27] Sadeghi Reineh, M., Fardadi, M., and Jabbari, F., 2017, "Thermal Control of SOFC: An Anti-Windup Approach for Maximizing Usable Power," IEEE Conference on Control Technology and Applications, Kohala Coast, Hawaii, Aug. 27–30, pp. 311–316.